

Analysis of the Mean Forcing Fields Simulated By the Two-Level, Mintz-Arakawa Atmospheric Model

W. LAWRENCE GATES—*The Rand Corporation, Santa Monica, Calif.*

ABSTRACT—The global distributions of the mean January surface wind stress, the net diabatic heating rate, and the net rate of moisture addition as simulated in a 30-day integration with the two-level, Mintz-Arakawa atmospheric general circulation model are presented. The latitudinal distributions of the zonal averages of these forcing fields are shown to be in reasonable agreement with the available observations. The most prominent discrepancies are evidently due to the model's simulation of excessive convective precipitation (and the associated convective latent heating) in the Tropics, especially in the Northern (winter) Hemisphere. The zone of simulated tropical precipitation extends some 15° poleward of the

observed position and results in a corresponding distortion of the field of evaporation-minus-precipitation (or moisture-addition rate).

In determining the monthly mean forcing fields, one must be particularly accurate in accumulating the (convective) precipitation rate during the integration; the customary use of 6-hourly fields results in a sampling error as large as 25 percent for even the zonally averaged rainfall. With the exception of a small sampling error in the mean rate of absorption of solar radiation, the components of the other forcing fields are satisfactorily determined by 6-hourly data.

1. INTRODUCTION

The two-level, Mintz-Arakawa model of the atmospheric general circulation is one of the more widely known formulations used in extended numerical simulations of global weather and climate. This model is the simplest in terms of the physical variables retained, while still explicitly treating the cyclone-scale motions—it addresses the wind, geopotential, and temperature at only two tropospheric levels, and the moisture at only the lower level. In addition, only the more important elements of the heat and hydrological balance are simulated at the earth's surface. As a result of this simplicity, the two-level Mintz-Arakawa model is an economical formulation for producing a climatic simulation, requiring only 26 min on an IBM 360/91 computer¹ to simulate 1 day. This simplicity and economy would be irrelevant, of course, were it not also a fact that this model has proven capable of reproducing the major features of the mean atmospheric circulation. For these reasons, the two-level Mintz-Arakawa model has been adopted as the major simulation tool of Rand's research program in climate dynamics, and a comprehensive documentation of the model has been prepared (Gates et al. 1971).

The atmosphere is driven primarily by the forcing functions representing the net heating and the net kinetic energy dissipation. Together with the distribution of the excess evaporation over precipitation and the boundary conditions at the surface, these source terms are ultimately responsible for the character of the mean circulation and climate. Since friction, heating, precipitation, and evap-

oration are not specified ahead of time in this model but are determined by the simulated circulation itself, the structure of the derived average forcing fields provides an important calibration of the modeling of the various physical processes that control the addition and removal of energy from the atmosphere. It is the purpose of this report to present the average source terms, as simulated by the two-level model for a single January, and to compare these with the available observations.

The mean source terms considered here are the averages during a 30-day integration, corresponding to the month of January, during which the only change from the documented or reference integration (Gates et al. 1971) was a reduction of 10 percent in the incoming solar radiation subject to scattering. This integration was used for the present analysis for reasons of convenience, and no discussion of its possible physical significance is given here. The average climatic variables such as pressure, temperature, cloudiness, and wind, simulated during the reference or control experiment itself, are presented elsewhere (Gates 1972).

2. THE FORCING FIELDS IN THE MODEL

The dynamics of the two-level, Mintz-Arakawa model are formulated in terms of a vertical independent variable σ , which is a scaled pressure coordinate given by

$$\sigma = \frac{(p - p_T)}{\pi} \quad (1)$$

where p is pressure, p_T is an assumed constant pressure at the tropopause ($p_T = 200$ mb, the top of the model atmosphere) and $\pi = p_s - p_T$, the difference between the

¹ Mention of a commercial product does not constitute an endorsement.

(variable) surface pressure, p_s and p_r . In terms of this coordinate, the basic dynamical equations may be written

$$\frac{\partial}{\partial t} (\pi \mathbf{V}) + \nabla(\pi \mathbf{V}, \mathbf{V}) + \frac{\partial}{\partial \sigma} (\pi \dot{\sigma} \mathbf{V}) + f \mathbf{k} \times \pi \mathbf{V} + \pi \nabla \phi + \sigma \pi \alpha \nabla \pi = \pi \mathbf{F}, \quad (2)$$

$$\frac{\partial}{\partial t} (\pi c_p T) + \nabla \cdot (\pi c_p T \mathbf{V}) + \frac{\partial}{\partial \sigma} (\pi c_p \dot{\sigma} T) - \pi \alpha \left(\sigma \frac{\partial \pi}{\partial t} + \sigma \mathbf{V} \cdot \nabla \pi + \pi \dot{\sigma} \right) = \pi \dot{H}, \quad (3)$$

$$\frac{\partial}{\partial t} (\pi q) + \nabla \cdot (\pi q \mathbf{V}) + \frac{\partial}{\partial \sigma} (\pi q \dot{\sigma}) = \pi \dot{Q}, \quad (4)$$

and

$$\frac{\partial \pi}{\partial t} + \nabla \cdot (\pi \mathbf{V}) + \frac{\partial}{\partial \sigma} (\pi \dot{\sigma}) = 0. \quad (5)$$

The operator $\nabla(\pi \mathbf{V}, \mathbf{V})$ is to be interpreted as $\mathbf{V}(\nabla \cdot \pi \mathbf{V}) + (\pi \mathbf{V} \cdot \nabla) \mathbf{V}$. Here, eq (2) is the vector equation of horizontal motion, eq (3) is the thermodynamic energy equation, and eq (4) and (5) are the continuity equations for moisture and mass, respectively. Together with the equations of state ($\alpha = RT/p$) and hydrostatic balance ($\partial \phi / \partial \sigma + \pi \alpha = 0$), these are the so-called "primitive" equations of the model, expressed in terms of the horizontal vector velocity, \mathbf{V} , the temperature, T , the specific volume, α , the mixing ratio, q , and the geopotential, ϕ , with the remaining symbols having their usual meanings.² Of principal concern here are the forcing terms on the right sides of eq (2)–(4), expressed in terms of the horizontal frictional force per unit mass, \mathbf{F} , the diabatic heating rate per unit mass, \dot{H} , and the rate of moisture addition per unit mass, \dot{Q} .

The boundary conditions accompanying this system are $\dot{\sigma} = d\sigma/dt = 0$ at both $\sigma = 0$ and $\sigma = 1$, $\phi = gz_s$ at the earth's surface, where z_s is the ground elevation ($z_s = 0$ over the ocean), and the assumptions of zero net heat flux between the atmosphere and an underlying land surface and of a prescribed temperature for an underlying ocean surface. Also prescribed in the model are the locations of sea ice and of ice-covered land, where the surface temperature is not allowed to rise above 0°C .

3. THE GLOBAL DISTRIBUTION OF THE SIMULATED FORCING FIELDS

The Net Frictional Force, \mathbf{F}

In the application of eq. (2) at the discrete model levels $\sigma = 1/4$ (level 1) and $\sigma = 3/4$ (level 3), the frictional force per unit mass is given by

$$\mathbf{F}_1 = -\mu \left(\frac{\partial \mathbf{V}}{\partial z} \right)_2 \frac{2g}{\pi} \quad (6)$$

and

$$\mathbf{F}_3 = -\mathbf{F}_1 - C_D \rho_4 \mathbf{V}_s (|\mathbf{V}_s| + G) \frac{2g}{\pi} \quad (7)$$

Here, \mathbf{F}_1 is an internal frictional force at level 1 proportional to the vertical stress and, hence, proportional to the vertical shear, $(\partial \mathbf{V} / \partial z)_2$, at level 2 (i.e., $\sigma = 1/2$). The term μ is an empirical coefficient ($\mu = 0.44$ mb/s), z is the vertical geometric height, and the factor $2g/\pi$ is the reciprocal of the mass per unit horizontal area in the upper and lower model layers. The frictional force at the lower level 3 (i.e., \mathbf{F}_3) consists of a component equal and opposite to \mathbf{F}_1 and a component representing the frictional force at the surface. Hence, the net frictional force, τ , on an atmospheric column in the model is given by

$$\tau = \mathbf{F}_1 + \mathbf{F}_3 = -C_D \rho_4 \mathbf{V}_s (|\mathbf{V}_s| + G) \frac{2g}{\pi} \quad (8)$$

where C_D is the surface drag coefficient, ρ_4 is the surface air density, \mathbf{V}_s is a measure of the surface wind ($\mathbf{V}_s = 0.7 \mathbf{V}_4$, where $\mathbf{V}_4 = 1/2 \mathbf{V}_3 - 1/2 \mathbf{V}_1$ is the extrapolated surface wind), and G is an empirical correction for gustiness ($G = 2.0$ m/s).

The force, τ , given by eq (8), therefore, represents the surface skin friction, or alternatively, $-\tau$ represents the drag of the earth on the atmosphere. The zonal and meridional components of the surface wind stress, $\tau_w \equiv -\tau(\pi/2g)$, are given, respectively, by

$$\tau_w^z = C_D \rho_4 u_s (|\mathbf{V}_s| + G) \quad (9)$$

and

$$\tau_w^y = C_D \rho_4 v_s (|\mathbf{V}_s| + G) \quad (10)$$

where $u_s = a \cos \varphi d\lambda/dt$ is the zonal surface wind component and $v_s = a d\varphi/dt$ is the meridional surface wind component, with φ the latitude and λ the longitude on a spherical earth of radius a .

In the model, the drag coefficient, C_D , is given by the following empirical expressions:

Over oceans

$$C_D = 0.0025$$

or

$$C_D = (0.0010 + 0.00007 |\mathbf{V}_s| \text{ s/m}) \quad (11)$$

whichever is smaller.

Over land or ice

$$C_D = 0.0020 + 0.0000012 z_s \text{ m}^{-1}. \quad (12)$$

Thus, the surface drag is velocity dependent over the oceans and varies between 0.001 and 0.0025. Over land (or ice), the drag depends only on the surface elevation, and varies between 0.002 over lowlands to about 0.007 over the highest mountains. For further details, see Gates et al. (1971).

The global distribution of the average zonal surface stress, τ_w^z , obtained from the January simulation is given in figure 1, which clearly shows the presence of the mean surface midlatitude westerlies and the mean easterlies of lower latitudes in both the winter and summer hemispheres. These stresses may be compared with those for December-January-February given by Hellerman (1967);

² In eq. (2), $f = [2\Omega + u/(a \cos \varphi)] \sin \varphi$, where Ω is the earth's rotation rate and a is its radius, u is the eastward wind speed, and φ is the latitude.

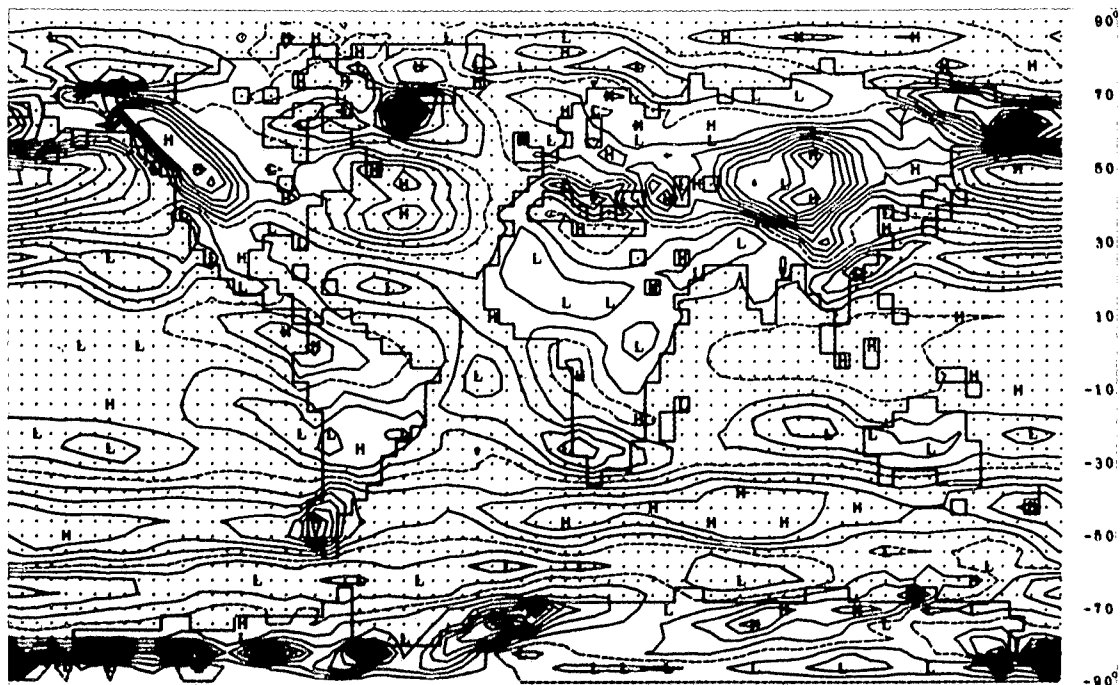


FIGURE 1.—The average zonal surface wind stress, τ_{λ}^{λ} , in a 30-day January simulation with the two-level, Mintz-Arakawa model. The 5°-longitude, 4°-latitude grid is shown over the oceans, with latitude given on the right. The symbols H and L denote maximum (positive, eastward) and minimum (negative, westward) stress. Isolines are drawn every 0.5 dynes \cdot cm $^{-2}$ ($0.5 \times 10^{-1} \text{N} \cdot \text{m}^{-2}$) with the zero isoline dashed. In the absence of isolines, the symbols H and L denote local relative stress maxima and minima.

the most systematic differences are over the North Pacific Ocean, where the maximum westerly and easterly stresses are simulated about 15° latitude north of their observed positions and are approximately 50 percent too strong. Over the remaining oceans, both the stress pattern and magnitude are in reasonably good agreement with Hellerman's data. Since Hellerman used a quadratic stress formulation similar to eq (9) to determine the stress from observed wind-rose data, this agreement reflects the general fidelity of at least the pattern of the simulated surface wind field. We may also note that the oceanic drag coefficient [eq (11)] assumes approximately the same values as the coefficient used by Hellerman.

Over the continents, we find the same general latitudinal dependence of the simulated zonal stress (fig. 1) as over the oceans; here, however, the height dependence of the drag coefficient, eq (12), has produced local maxima of the stress over the Rocky, Andes, and Himalaya Mountains and has systematically increased the stress over Greenland and Antarctica. The fidelity of these continental stress distributions over land is unknown in the absence of suitable observations, although the height dependence of C_D in eq (12) was taken from the drag coefficients suggested by Cressman (1960).

The corresponding distribution of the average meridional surface stress τ_{ϕ}^{ϕ} obtained from the January simulation is shown in figure 2. Here the agreement over the oceans with the data of Hellerman (1967) is only fair; the simulated northward stress over the northeastern North Pacific and Atlantic Oceans is approximately twice the strength of that observed, whereas the observed broad band of southward stress in the Northern Hemisphere subtropical oceans is not well simulated in the

model integration. In the Southern Hemisphere, the maxima of northward stress just west of South America, Africa, and Australia at about 20° to 30°S correspond well with observation. Over the continents, the influence of topography is again noticeable in the presence of meridional stress maxima over the Rocky, Andes, and Himalaya Mountains, as well as over portions of Greenland and Antarctica. These average patterns of meridional stress reflect the standing components of the mean meridional circulation, which generally consist, in the Northern Hemisphere, of a southward flow over the relatively cold continents with compensating northward flow over the intermediate warmer oceans. In the Southern Hemisphere, the summer (January) meridional circulation is dominated by the subtropical oceanic anticyclones.

Although it is the force, \mathbf{F} , that serves as a momentum source (or sink) in the model's equation of motion [eq (2)], the frictional dissipation of kinetic energy is given by $\mathbf{V} \cdot \mathbf{F}$. This includes dissipation at levels 1 and 3, with the latter having a component dependent upon the surface wind, \mathbf{V}_s , through eq (7). Although it is thus not relevant to the model's energy budget (to be considered later), the surface dissipation, $\mathbf{V}_s \cdot \boldsymbol{\tau}_s$, alone has a global mean of 1.4 W \cdot m $^{-2}$ in the present simulation. This value compares well with the 1.5 W \cdot m $^{-2}$ found for the Northern Hemisphere spring by Ellsaesser (1969) using data from Kung (1963).

The Net Diabatic Heating Rate, \dot{H}

When the thermodynamic energy equation [eq (3)] is applied at level 1 ($\sigma=1/4$) and level 3 ($\sigma=3/4$), the diabatic heating rates, \dot{H}_1 and \dot{H}_3 , are given in terms of temperature

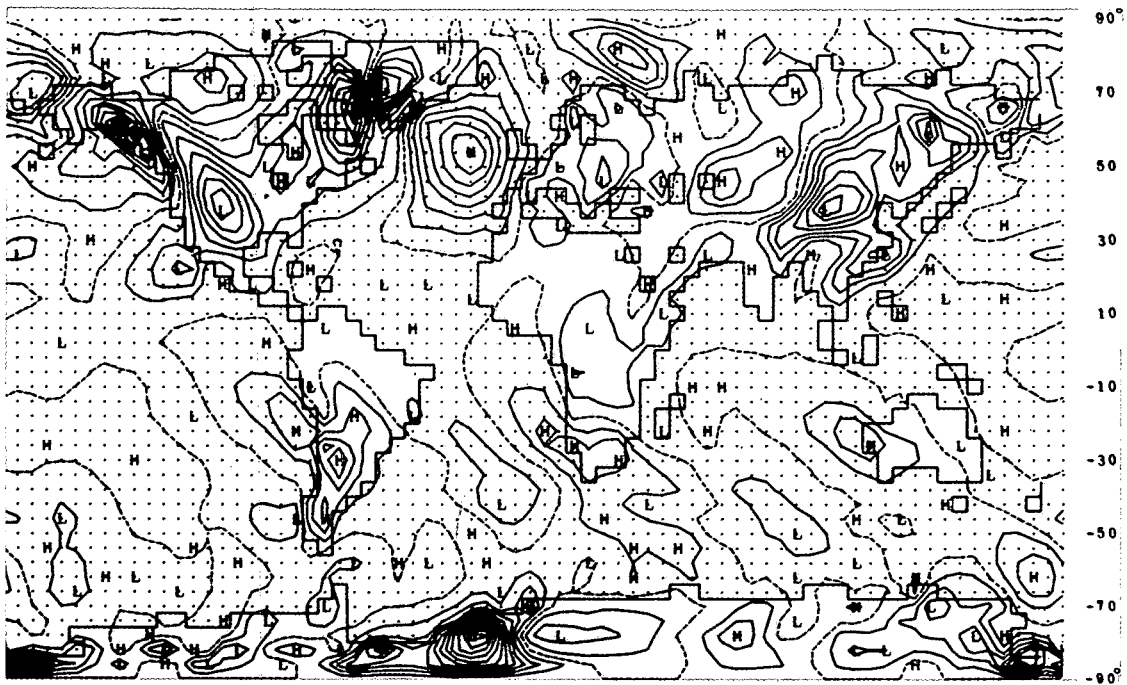


FIGURE 2.—Same as figure 1 for the average meridional surface wind stress, τ_w^y , with the positive (H) components directed northward.

change by

$$\dot{H}_1 = (A_1 + R_2 - R_0) \frac{2g}{\pi c_p} + \Delta T_{1,CM} + \Delta T_{1,CP} \quad (13)$$

and

$$\dot{H}_3 = (A_3 + R_4 - R_2 + \Gamma) \frac{2g}{\pi c_p} + \Delta T_{3,CM} + \Delta T_{3,CP} + \Delta T_{3,LS} \quad (14)$$

Here, A_1 and A_3 are the net short-wave radiation absorbed at levels 1 and 3, and R_0 , R_2 , and R_4 are the net upward long-wave radiation emitted from the levels 0 ($\sigma=0$), 2 ($\sigma=1/2$), and 4 ($\sigma=1$), respectively. Hence, $A_1 + R_2 - R_0$ represents the net radiation absorbed in the upper model layer (identified with level 1), and $A_3 + R_4 - R_2$ is the net radiation absorbed in the lower layer (identified with level 3). The factor $2g/\pi c_p$ converts the heating rates to the equivalent rate of change of temperature.

The term Γ represents the upward flux of sensible heat from the earth's surface and is given by

$$\Gamma = C_D \rho_4 c_p (|\mathbf{V}_s| + G)(T_g - T_4) \quad (15)$$

where T_g is the ground (or ocean surface) temperature, T_4 is the surface air temperature, and the other terms are as in eq (8)–(12). The remaining terms in eq (13) and (14) are the rates of temperature change due to the so-called midlevel moist convection (CM), penetrating moist convection (CP), and large-scale condensation (LS). The two forms of moist convection are parameterized at both levels of the model in terms of the vertical gradients of the total heat or static energy ($c_p T + gz + Lq$), whereas the large-scale condensation depends upon the moisture condensed as a result of supersaturation at level 3 only. Details of these parameterizations are given by Gates et al. (1971).

The net heating rate of an atmospheric column in the model may thus be written

$$\mathcal{H} = (\dot{H}_1 + \dot{H}_3) \frac{\pi c_p}{2g} = A_1 + A_3 + R_4 - R_0 + \Gamma + C_1 + C_3 + (\text{PREC}) \frac{L\pi}{2g} \quad (16)$$

where $C_1 = (\Delta T_{1,CM} + \Delta T_{1,CP}) \pi c_p / 2g$ is the upper level convective heating, $C_3 = (\Delta T_{3,CM} + \Delta T_{3,CP}) \pi c_p / 2g$ is the lower level convective heating, PREC is the large-scale condensation rate, and L is the latent heat of condensation.

The global distribution of the average net heating, \mathcal{H} , obtained from the 30-day January simulation is shown in figure 3. We note that over the continents of the Northern Hemisphere there is virtually no average net heating of the atmosphere. This may be influenced by the assumed lower boundary condition of zero net heat flux at the earth's bare-land or ice-covered surfaces; that is,

$$R_4 + \Gamma + H_E - S_g - I = 0 \quad (17)$$

where H_E is the flux of latent heat due to surface evaporation, S_g is the short-wave radiation absorbed at the land or ice surface, and I is the upward heat flux by conduction through sea ice. This equilibrium is, in fact, used to determine the appropriate ground temperature, T_g , upon which the terms R_4 , Γ , and I depend. Thus, over land, the sensible and latent heat fluxes are used in effect to balance the surface heat budget, whereas over the oceans, where the surface temperature is held constant, the condition given by eq. (17) does not apply. This results in an average net atmospheric heating where the prescribed sea-surface temperature is higher than the simulated air temperature, a condition that occurs over much of the

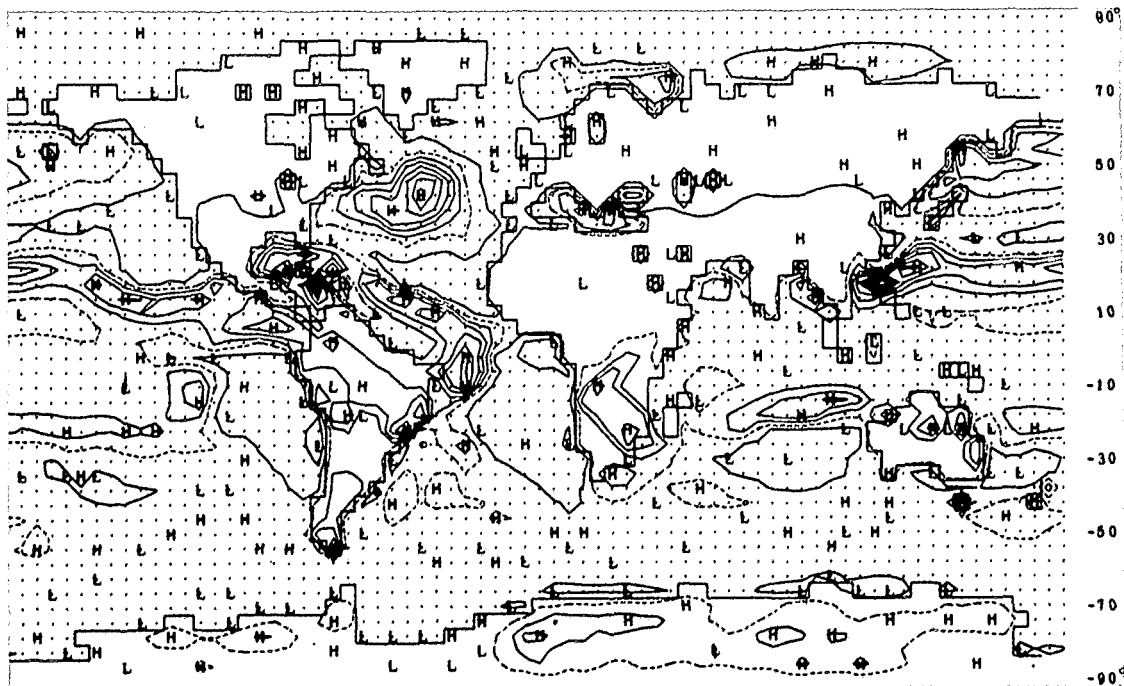


FIGURE 3.—The average net diabatic heating rate of the atmosphere in a January simulation. The symbols H and L denote maximum (positive, warming) and minimum (negative, cooling) diabatic heating rates. The isolines are drawn every 200 ly/day with the zero isoline dashed. In the absence of isolines, the symbols H and L denote local relative heating rate maxima and minima.

world's oceans, as may be seen in figure 3. This is particularly marked in the western portions of the North Atlantic and North Pacific Oceans, where the net heating exceeds 1000 ly/day. Over most of the Southern Hemisphere oceans, the average net heating rate is negative and of the order of -100 ly/day, with relatively weak gradients.

The dominant influence on the pattern of net heating in figure 3 is the distribution of the simulated convective condensation heating, C_1 and C_3 . Because these terms depend, in part, upon the air-sea temperature difference and on the available moisture in the air, it is not surprising that the net heating bears a resemblance to the distributions of both the sensible heat flux and the surface evaporation (as discussed below). It is clear from these data that the oceans exert an important controlling influence on the model atmosphere's net heat balance and, hence, on the simulated mean circulation.

The Net Rate of Moisture Addition, $E - P$

When the moisture continuity equation [eq (4)] is applied at level 3 in the model, the moisture-source term, \dot{Q} is given by the difference between surface evaporation and total precipitation, since it is assumed that all of the atmospheric moisture is carried at this single level. Thus,

$$\dot{Q} = \dot{Q}_3 = E - P \quad (18)$$

where the surface evaporation, E , is given by

$$E = C_D \rho_4 \rho_w^{-1} (|\mathbf{V}_s| + G)(q_s - q_a). \quad (19)$$

Here, ρ_w is the density of water, q_a is the mixing ratio of the air just above the ground, and q_s is a mixing ratio for

the ground surface itself [which includes a measure of ground wetness; see Gates et al. (1971) for details]. The total precipitation, P , is assumed equal to the total condensation and consists of the moisture released by both the large-scale and convective processes. Thus, we may write

$$P = P_{LS} + P_C \quad (20)$$

where the large-scale precipitation (or condensation) rate is given by

$$P_{LS} = (\text{PREC}) \frac{\pi}{2g\rho_w}, \quad (21)$$

the convective precipitation (or condensation) rate is given by

$$P_C = \frac{C_1 + C_3}{L\rho_w}. \quad (22)$$

In terms of the moisture released and the consequent temperature change, we may write

$$\text{PREC} = \Delta q_{3,LS} = \Delta T_{3,LS} \left(\frac{c_p}{L} \right) \quad (23)$$

and

$$\begin{aligned} C_1 + C_3 &= (\Delta q_{3,CM} + \Delta q_{3,CP}) \frac{\pi L}{2g} \\ &= (\Delta T_{1,CM} + \Delta T_{1,CP} + \Delta T_{3,CM} + \Delta T_{3,CP}) \frac{\pi c_p}{2g}. \end{aligned} \quad (24)$$

The moisture temporarily stored in the air as cloud is not considered in the present model, although measures of ground wetness and runoff are included. We may also note that all precipitation is assumed to fall as rain; snow cover is prescribed (as a function of latitude) only for the purpose of determining the surface albedo.

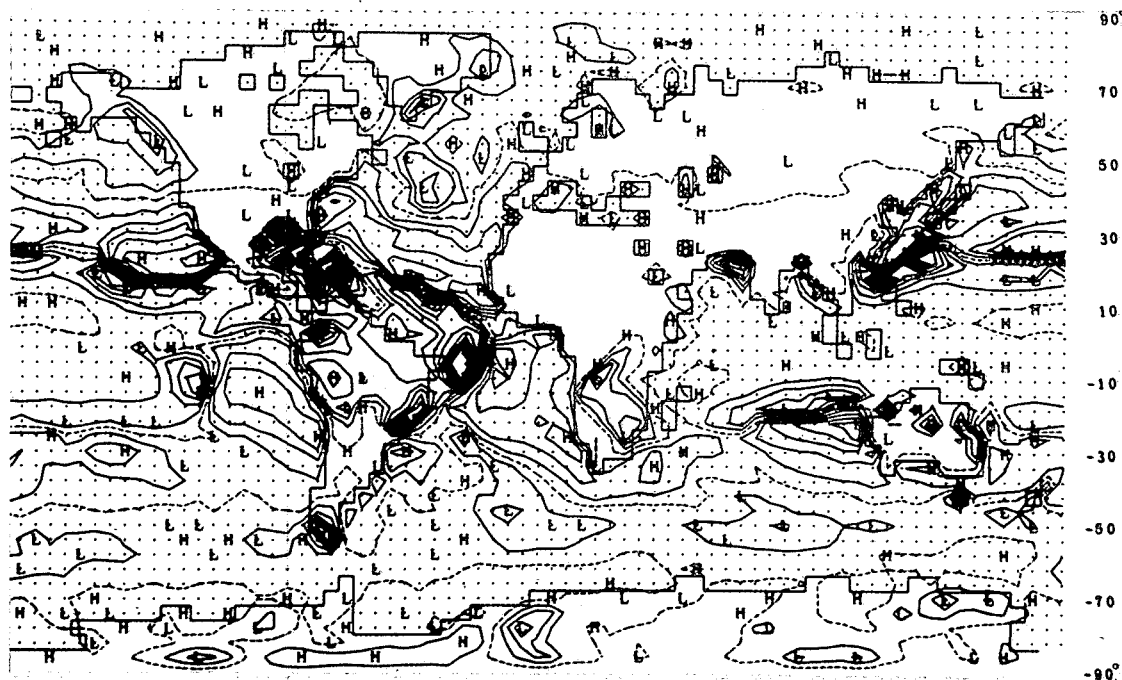


FIGURE 4.—The average net rate of moisture addition ($E-P$) in a January simulation. The symbols H and L denote maximum (positive) and minimum (negative) moisture addition rates. The isolines are drawn every 2 mm/day with the zero isoline dashed. In the absence of isolines, the symbols H and L denote local relative moisture addition rate maxima and minima.

The global distribution of the average net rate of moisture addition, $\dot{Q}=E-P$, obtained from the 30-day simulation, is shown in figure 4. This field reflects the presence of the lower latitude precipitation maxima over the oceans (principally convective precipitation) and, to this extent, bears an inverse resemblance to the distribution of the average net heating rate in figure 3. In the subtropics, the relatively high evaporation over the oceans is the dominant moisture source, while in the higher latitudes the large-scale precipitation serves as the principal moisture sink. Over the North Pacific and North Atlantic Oceans, this distribution is in broad agreement with that derived from observations for the northern winter by Jacobs (1951), although his maxima are only about half those simulated here. Over the continents in the winter hemisphere, there is apparently little net contribution to the moisture balance. In the simulation, as in nature, the oceans provide most of the moisture and receive the bulk of the precipitation in return.

4. THE ZONAL-AVERAGE SOURCE TERMS AND THEIR COMPARISON WITH OBSERVATION

The average global distributions of the net friction, heating, and moisture sources shown in figures 1-4 correspond in general with those few observational studies available. None of these quantities, however, is directly observed, and the degree of empiricism in the available data is substantial. The present simulations, moreover, are for a single January and may therefore differ from the longer term average behavior of the model. For these reasons, a detailed analysis of the geographical distribu-

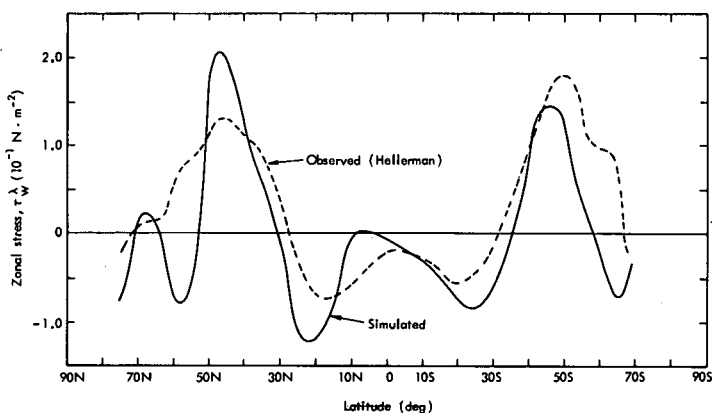


FIGURE 5.—The latitudinal distribution of the zonal average of the surface zonal frictional stress simulated for January over the oceans (full lines). The observed oceanic zonal average shown by the dashed lines is from the December-January-February data of Hellerman (1967).

tions of \mathbf{F} , \dot{H} , and \dot{Q} does not seem warranted at this time. The simulated *zonal averages*, on the other hand, may be more reliable and may be usefully compared with observations.

The Surface Frictional Stress Components

The latitudinal distribution of the zonal average of the zonal stress component, τ_w^λ , is given in figure 5, as obtained from the data of figure 1. For comparison with the corresponding observed data for December-January-February given by Hellerman (1967), these data have been averaged only over the oceans. While the positions of the midlatitude westerlies and subtropical easterlies are

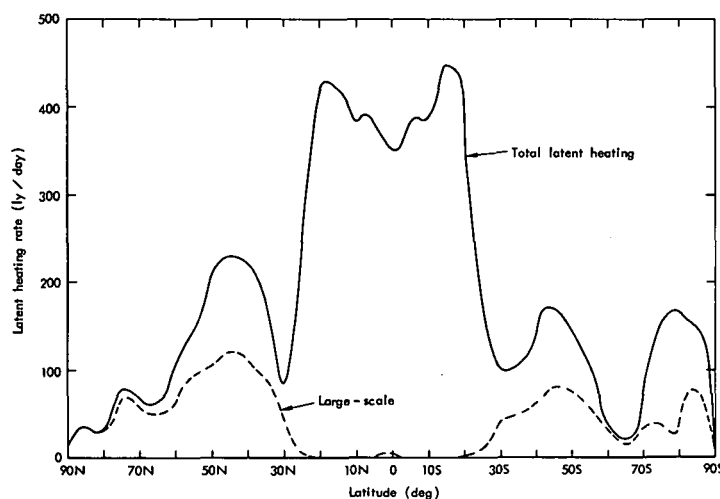


FIGURE 6.—The latitudinal distribution of the zonal average of the simulated January latent heating rate due to large-scale condensation, given by (PREC) $L\pi/2g$, and the total latent heating rate due to both large-scale and convective condensation ($C_1 + C_3$) as in eq (16).

approximately correct, their strengths are overestimated by about 50 percent in the Northern Hemisphere. A similar error is present in the simulated zonal winds in the troposphere (Gates 1972). Closer inspection of figure 5 shows that the subtropical easterlies are about 5° poleward of their observed positions in both hemispheres. This small but systematic error may be associated with the model's calculation of the subtropical latent heating at latitudes systematically poleward of the observed positions (figs. 6, 10). If this oceanic zonal wind stress was used to drive the ocean circulation, in which the latitudinal variation of the zonal stress controls both the location and transport of the semipermanent ocean current systems, the major oceanic gyres would be reproduced in approximately their correct positions but with about 50 percent greater intensity than would be produced if the observed mean stress was used. Such systematic simulation errors of the atmospheric model should be corrected before they are passed on to a coupled ocean circulation.

Although less familiar to oceanographers, the zonal variation of the mean meridional surface wind stress τ_w^y of figure 2 could equally well drive an ocean circulation because the effective dynamical coupling is through curl τ_w . From figure 2, however, we note that only over the North Atlantic would this stress contribute significantly to the (cyclonic) ocean circulation; over most of the world's oceans, the zonal variation of τ_w^y (fig. 2) is smaller than the meridional variation of τ_w^x (fig. 1).

The Components of the Net Heating Rate

The latitudinal distributions of the zonal average of the components of the net heating [eq (16)] are shown in Figures 6–9. The total latent heat, $C_1 + C_3 + (\text{PREC}) L\pi/2g$, released by the model's condensation processes is shown in figure 6, together with that released by the large-scale condensation alone. The convective processes, represented by the difference between these curves, are seen to be the more important for total atmospheric heating and completely dominate the heating rates in the lower latitudes.

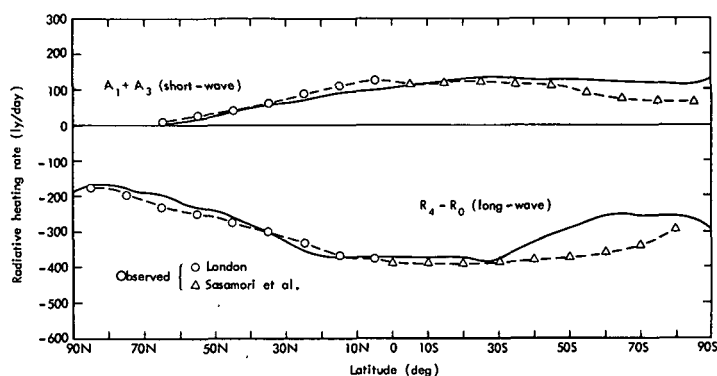


FIGURE 7.—The latitudinal distribution of the zonal average of the simulated January rate of absorption of solar radiation by water vapor and clouds, given by $A_1 + A_3$ as in eq (16) (upper curve), and the net rate of long-wave radiative cooling as given by $R_4 - R_0$ (lower curve). The corresponding observed data in the Northern Hemisphere (open circles) are from London (1957), and those in the Southern Hemisphere (open triangles) are from Sasamori et al. (1971), based on data of Budyko (1963).

In the middle latitudes of both hemispheres, the convective and large-scale condensation heating make approximately equal contributions. North of about 60°N , nearly all of the simulated latent heating is the result of large-scale (rather than convective) condensation. Over the globe, the average latent heating rate is 238 ly/day, of which 201 ly/day are from convective condensation alone.

The dominance of large-scale condensation noted above probably exists in the higher latitudes of the Southern Hemisphere as well. The relatively large amount of convective latent heating actually simulated between 70° and 90°S (fig. 6) is the result of an inadvertent (and only recently discovered) error in the model's treatment of the albedo of snow and ice. This error has caused the albedo over Antarctica in particular to be underestimated by about 0.4, giving increased absorption of solar radiation at the surface. This has in turn resulted in anomalously high surface temperatures, from which the simulation of convection has followed by virtue of the decreased vertical stability. The results of this albedo error are also noticeable in the simulated fields of radiative heating, sensible heat flux, precipitation, and evaporation discussed later. (See also Gates 1972.)

Figure 7 shows the latitudinal distribution of the net rate of short-wave (solar) radiation absorption by water vapor and clouds in the atmospheric column; in eq. (16), this is given by $A_1 + A_3$, the sum of the net insolation absorption rates in the upper and lower model layers. The model's rate of absorption is close to, but systematically less than, the observed data given by London (1957) for the Northern Hemisphere winter. In the Southern Hemisphere, the simulated short-wave radiative heating rate is significantly greater than that given for January by Sasamori et al. (1971). Some of this discrepancy, especially at the higher southern latitudes, is probably due to the model's error in the albedo of ice, which permits about twice as much solar radiation to be absorbed at the surface as is observed.

Also shown in figure 7 is the latitudinal distribution of the net rate of long-wave radiative heating, given by $R_4 -$

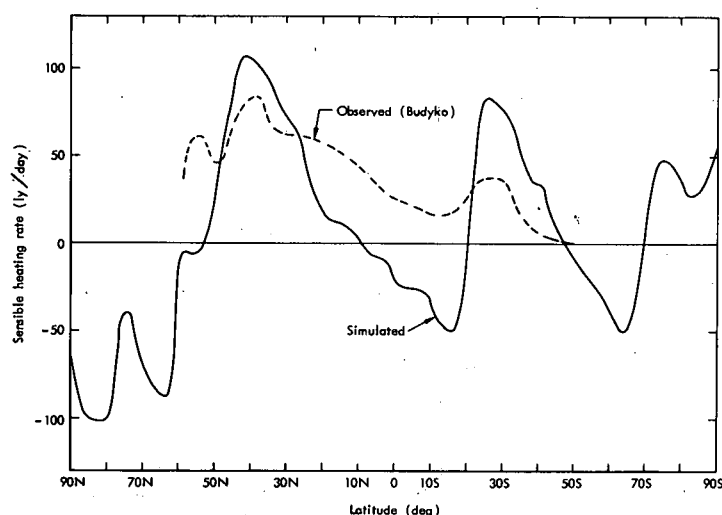


FIGURE 8.—The latitudinal distribution of the zonal average of the simulated January heat flux due to the vertical (turbulent) transfer of sensible heat, as given by Γ in eq (15). The observations are from Schutz and Gates (1971), based on data of Budyko (1963).

R_0 in eq. (16), the difference between the long-wave emission from the surface and that from the top of the model atmosphere. Since $R_4 - R_0 < 0$, the long-wave radiation produces a net cooling of the atmospheric column. For the January conditions simulated, there is no solar radiation absorbed north of about 70°N; over the remainder of the globe, however, both the short- and long-wave radiative heating are affected by the simulated distributions of water vapor and cloudiness. The agreement with the data of London (1957) and of Sasamori et al. (1971) is good north of 30°S; south of this latitude there is a systematic underestimation of the long-wave cooling rate by about 30 percent.

The maximum cooling rate given by the total radiative heating ($A_1 + A_3 + R_4 - R_0$) occurs in the northern subtropical latitudes, and agrees reasonably well with observation. The minimum heating simulated in the higher latitudes of the Southern Hemisphere, however, is an exception. Here, the model's ice-albedo error noted earlier may be the cause of the discrepancy south of 65°S. Over the southern oceans (40° to 60°S), however, there are also systematic errors in the simulated surface balance that appear to be due to the model's underestimation of the cloudiness (Gates 1972). Over the globe, the average radiational heating rate is -232 ly/day, with averages of -323 ly/day and 91 ly/day for the long-wave and short-wave heating rates, respectively.

The latitudinal distribution of the simulated zonal average heating rate, Γ , due to the vertical (turbulent) flux of sensible heat from the surface is given in figure 8. The prominent positive heat flux between approximately 20° and 50°N is due to the large upward heat flux over the oceans off the east coasts of Asia and North America, whereas the positive flux between approximately 20° and 40°S is due to the upward flux over the relatively warm continents of the Southern (summer) Hemisphere. The downward (negative) fluxes near the Equator and near 60°S may be due to the relatively cool ocean surface

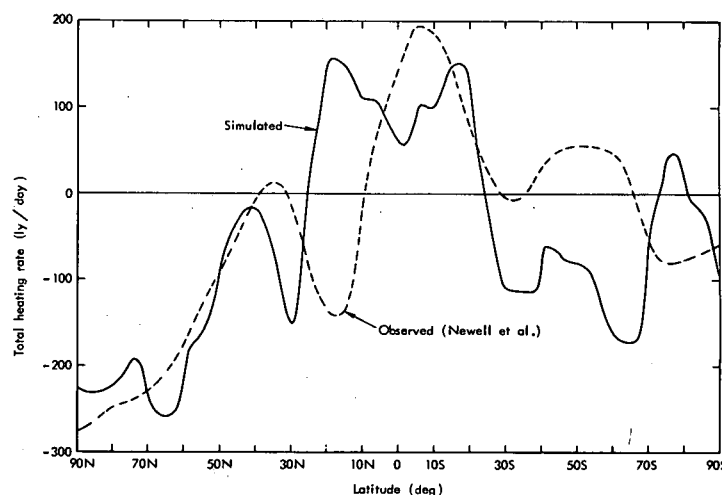


FIGURE 9.—The latitudinal distribution of the zonal average of the simulated January total (net) heating rate of the atmosphere, as given by \mathcal{H} in eq (16). The dashed curve is the observed total heating rate for December-January-February given by Newell et al. (1970).

temperatures prescribed at these latitudes, while the negative flux at high northern latitudes is due to the formation of a ground inversion ($T_g < T_a$) over the land and sea ice in the absence of significant solar radiation in January. The global average sensible heat flux is 13 ly/day.

Comparing the simulated values with the observed distribution of the zonal average sensible heat flux given by Schutz and Gates (1971), based upon data of Budyko (1963), we see that the midlatitude maxima are reasonably well depicted (although overestimated) in the simulation. More serious is the model's replacement of the low but positive sensible heat flux in latitudes 10°N to 20°S by a downward (negative) flux. The cause of this discrepancy is the excessive heating of the air by the convective condensation, which has made the air warm enough to reverse the sign of the (usual) surface sensible heat flux. We may also note the simulation of an upward sensible heat flux south of about 70°S; this feature is likely due to the high surface temperatures over Antarctica, caused by the model's underestimation of the albedo of ice noted earlier.

Figure 9 shows the latitudinal distribution of the zonal average of the total heating rate of the model atmospheric column ($p \geq 200$ mb), as given by \mathcal{H} in eq (16); this is the sum of the distributions shown in figures 6–8 (or the zonal average of the data of fig. 3). The principal simulated January heating of the atmosphere is seen to occur between about 25°N and 25°S and is approximately symmetric about the Equator. Comparison with figure 6 shows that the distribution is strongly influenced by the latent heat released through convective precipitation. Comparison with the observed net heating of the atmosphere given by Newell et al. (1970) indicates that the simulation in the Northern Hemisphere may be considered satisfactory, except for the model's northward displacement, by some 15°, of the subtropical zone of minimum heating. In the Southern Hemisphere, the

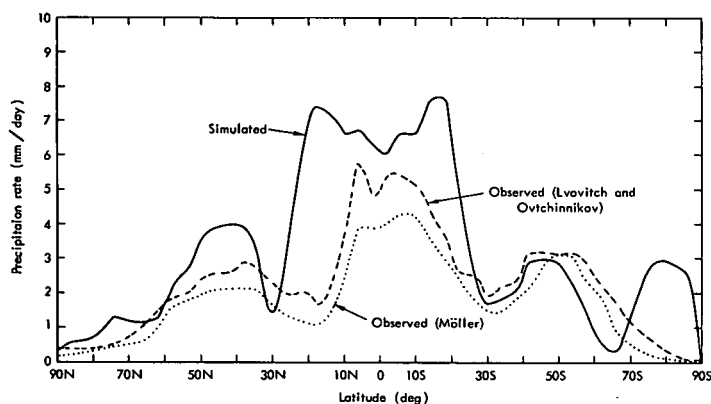


FIGURE 10.—The latitudinal distribution of the zonal average of the simulated January total precipitation rate, as given by P in eq (20). The dashed curve is the observed precipitation rate for December-January-February as given by Schutz and Gates (1971) using data of Lvovitch and Ovtchinnikov (1964), and the dotted curve is from the December-January-February precipitation data given by Möller (1951).

agreement is much less satisfactory, although the simulated and observed heating curves have generally similar features. The positive total heating simulated around 70°S is due to both the excessive short-wave absorption and the excessive convective latent heating noted earlier. In the global average, the computed net heating rate is -16 ly/day; this corresponds to a cooling of the entire atmosphere over the 30-day simulation of about 1°C, and is not inconsistent with the conditions of this particular experiment. (See sec. 1.)

The Components of the Moisture Balance

The latitudinal distribution of the zonal average of the simulated January precipitation is shown in figure 10. Here we see that the total precipitation (equal to the total condensation in the model) is a reasonably accurate approximation to the observed December-January-February precipitation as given by both Lvovitch and Ovtchinnikov (1964) and Möller (1951) in the middle and high latitudes of both hemispheres. (An exception occurs over Antarctica, where the model's simulation is doubtful due to the albedo error noted earlier.) Between about 30°N and 30°S, however, the observed precipitation is overestimated in the simulation by approximately 50 percent, with the tropical rainfall maxima displaced 10°–15° toward the poles. This error is primarily responsible for the simulated global average January precipitation rate of 4.11 mm/day being so far above the observed rate of 2.94 mm/day [from the data of Lvovitch and Ovtchinnikov (1964)] or 2.20 mm/day [from the data of Möller (1951)].

The simulated precipitation in figure 10 is proportional to the total latent heating in figure 6, with a heating rate of 100 ly/day corresponding to a precipitation (condensation) rate of approximately 1.72 mm/day. The excessive precipitation modeled in the Tropics is thus seen to be due almost entirely to convective processes, just as was the total heating of figure 9. An improvement in the parameterization of convection could therefore be expected to aid both the precipitation and heating-rate simulations considerably.

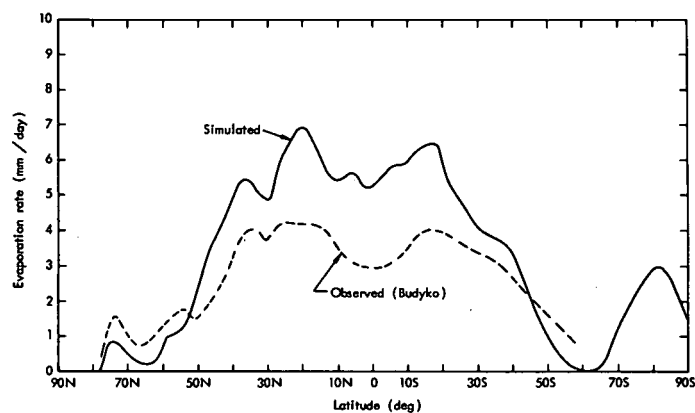


FIGURE 11.—The latitudinal distribution of the zonal average of the simulated January evaporation rate, as given by E in eq (19). The dashed curve is the observed January evaporation rate from Schutz and Gates (1971) based on data of Budyko (1963).

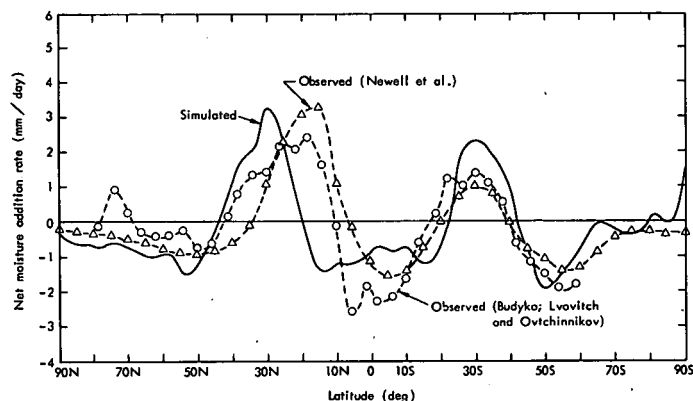


FIGURE 12.—The latitudinal distribution of the zonal average of the simulated January net moisture addition rate, $E-P$. The dashed curve with open triangles is the observed rate given by Newell et al. (1970) using data from various sources, whereas that with open circles is the observed distribution according to the data of Budyko (1963), as summarized by Schutz and Gates (1971), and of Lvovitch and Ovtchinnikov (1964).

The latitudinal distribution of the zonal average January evaporation, both as simulated and as given by Schutz and Gates (1971) based on the data of Budyko (1963), is given in figure 11. As with the precipitation, we see that between approximately 30°N and 30°S the simulated evaporation rate is about 50 percent greater than that observed. Like the precipitation error, this discrepancy may be mainly due to convection, with the surface evaporation attempting to moisten the atmosphere made too dry by excessive rainfall. It is known that the simulated relative humidity at level 3, for example, is only about half that observed at 800 mb between the latitudes 30°N and 20°S (Gates, 1972). Such a discrepancy would be sufficient to explain the evaporation error, since the model's mixing ratio, q_3 , depends primarily upon the level-3 relative humidity and the ground wetness (Gates et al. 1971.) The large evaporation rate simulated south of 70°S, like the precipitation (fig. 10) and sensible heat flux (fig. 8), is due to the excessively high surface temperatures over the Antarctic ice (Gates 1972).

The latitudinal distribution of the zonal average of the difference $E-P$, the net rate of moisture addition to the atmospheric column, is shown in figure 12 as simulated

for January, together with two measures of the observed distribution. The simulation may generally be considered a satisfactory approximation to observation. The subtropics near 30°N are seen to be the atmosphere's primary January moisture source, with the region around 30°S a secondary source. The simulated $E-P$ maximum in the Northern Hemisphere, however, is displaced approximately 10° north of the observed, due to the excessive precipitation simulated between 10°N and 25°N (fig. 10). In the equatorial region, the simulated negative $E-P$ is only about half that observed; this is due to the model's excessive evaporation in this region, as noted earlier (fig. 11). On the global average, the January evaporation and precipitation very nearly balance when averaged over the 30-day simulation, with a net $E-P$ of only -0.02 mm/day.

5. SUMMARY AND CONCLUSIONS

From the January simulation summarized here, it has been shown that the two-level, Mintz-Arakawa, model is capable of depicting the average forcing or source fields for momentum, heat, and moisture with reasonable accuracy. The simulated surface stress (or net frictional force on an atmospheric column) agrees fairly well with the general pattern of observed stress derived from surface-wind observations, although the magnitude of the stress is systematically overestimated. The simulated net heating rate of an atmospheric column shows fair agreement with observation but suffers from an excessive latent heating rate in the Tropics because of the model's apparent overcalculation of convective condensation. The sensible heat flux is also in error in the Tropics; here, the simulated flux is in fact opposite in sign to that observed. The net long- and short-wave heating rates for the atmospheric column agree reasonably well with observation, but here too there are some systematic errors.

Although an analysis of the model's simulation of the global January climate is given elsewhere (Gates 1972), the present simulation of the primary forcing fields F , \bar{H} , and \bar{Q} of the system [eq (2)–(4)] is sufficiently accurate to lead one to expect a reasonably satisfactory simulation of the average climatic elements such as pressure, temperature, humidity, and wind. The most prominent simulation error that appears to have significantly affected the forcing fields is the model's calculation of maximum (convective) precipitation at about 20°N and 20°S, rather than at the observed locations near 5°N and 5°S. Since the sensible and net radiational heating errors are relatively small (figs. 7, 8), the model's overestimation of the convective diabatic heating rate between 20°N and 20°S is apparently balanced by correspondingly enhanced mean upward vertical motions. The model is known to characteristically simulate too strong a Hadley circulation in both hemispheres (Gates 1972) and to systematically displace the Northern (winter) Hemisphere cell poleward by about 15° latitude. These errors tend to increase the mean meridional heating gradient, especially in the Northern Hemisphere. The resultant increased midlatitude baroclinicity may therefore be a cause of the excessive strength of the simulated zonal winds and of the associated excessive strength

of the midlatitude cyclones. A complete analysis of the simulated circulation's energy budget and its partitioning into mean and eddy components in both space and time is necessary to verify this conjecture, however.

A second systematic error noted at high southern latitudes is the model's simulation of too much absorbed solar radiation, too much (convective) precipitation and evaporation, and an upward sensible heat flux. These discrepancies are believed due to an inadvertent error in the albedo of ice and are not considered characteristic of the model itself. It may also be noted that the present results have been derived from a single 30-day January integration, and not from the average of many such January simulations. The year-to-year variations produced by the model clearly need to be examined before a definitive assessment can be made of the accuracy of the simulated climate.

APPENDIX

Effects of Sampling Frequency On the Estimation of the Mean Forcing Fields

The components of the average heating and moisture-addition rates discussed in this paper have been determined from the 30-day net accumulation of the various terms, with the accumulation updated every time the components are computed in the program (every $\frac{1}{2}$ hr). These fields have, therefore, been determined as accurately as they could be with the present model. For many climatological variables, however, a less frequent sampling is sufficient to determine a reliable monthly mean. In the present model simulations, a basic set of meteorological variables is normally saved on a history tape every 6 hr, from which the various components of the heating, for example, may be determined by reentering the appropriate portion of the program at that time. As anticipated, the 6-hr sampling frequency was found to determine with sufficient accuracy the simulated January average pressure, temperature, and wind distributions (Gates 1972), as well as quantities involving only simple manipulations of these basic variables. It was less clear, however, that the net forcing fields for heat, \bar{H} , and moisture, \bar{Q} , would be as accurately portrayed by 6-hourly sampling. For this reason, the averages of these fields were determined with several sampling intervals over a selected 10-day interval of the January simulation, and the results are summarized below.

Of the components of the heating rate \bar{H} [eq (16)], the distributions of the net long-wave radiative cooling, $R_i - R_o$, the sensible heat flux, Γ , and the latent heating due to large-scale condensation, (PREC) $L\pi/2g$, showed no significant differences in the cases of $\frac{1}{2}$ -hr and 6-hr sampling frequencies (480 and 40 samples, respectively, during the 10-day interval). The heating rate due to absorbed solar radiation, $A_i + A_s$, however, displays a small but noticeable change when sampled every 6 hr rather than every $\frac{1}{2}$ hr, as shown in figures 13 and 14. This error takes the form of a spurious enhancement of a 90° longitude zonal harmonic tied to the sun's local position at sampling times. When sampled every 12 hr (not shown), this sampling error appears as a 180° longitude harmonic

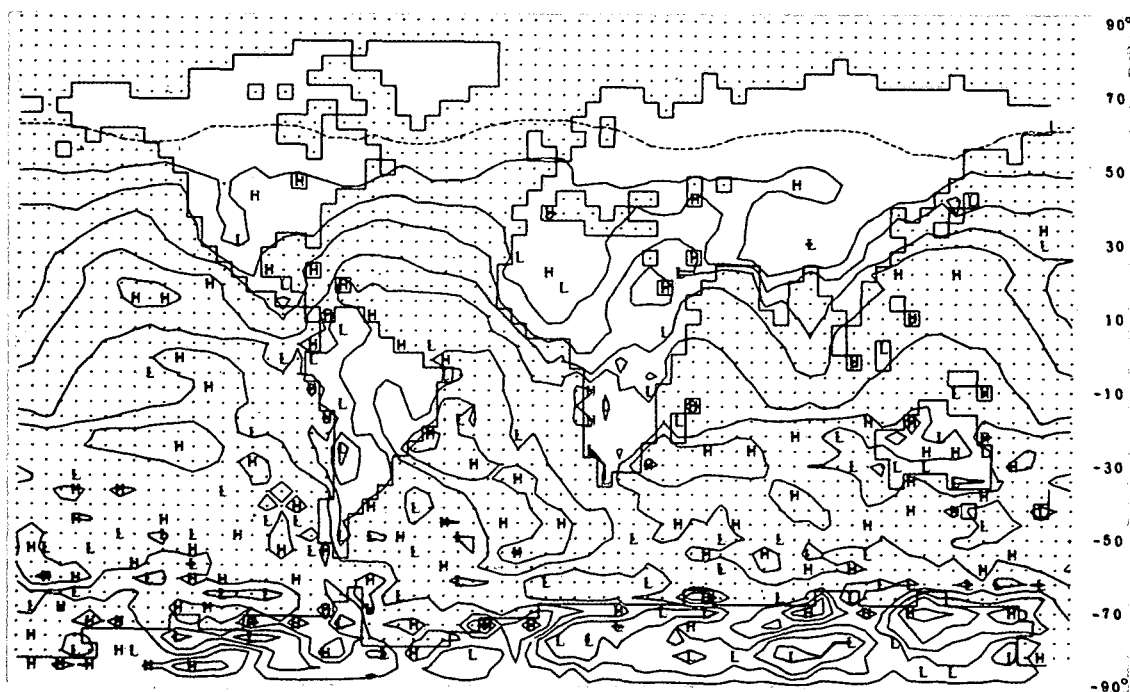


FIGURE 13.—The average rate of short-wave heating during 10 days of a January simulation, as given by sampling every 6 hr. The isolines are at 200 ly/day intervals, with the 100 ly/day isoline dashed. The symbols H and L denote local relative maxima and minima.

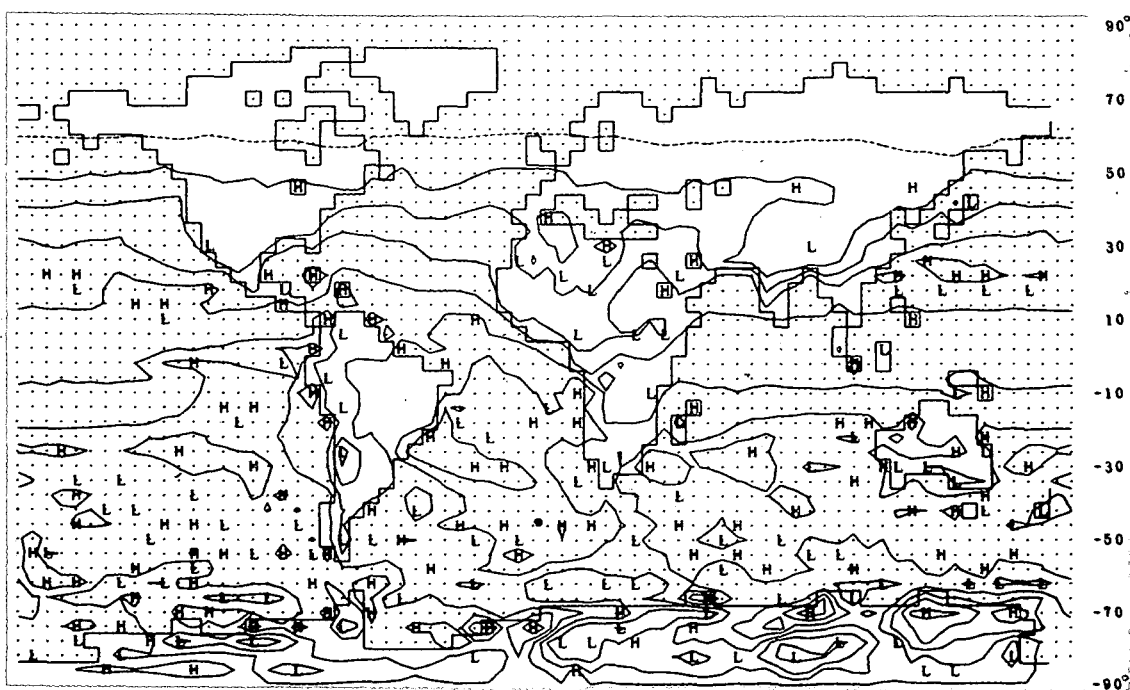


FIGURE 14.—Same as figure 13 for a sampling every 1/2 hr (the program's frequency of radiation calculation).

of larger amplitude; in the case of 24-hr sampling, there is no short-wave absorption at all over those parts of the earth that are (always) in darkness at sampling time. To minimize this sampling error, one should ensure that the product of the sampling interval and the angular rotation rate of the earth ($15^\circ/\text{hr}$) is not an integral multiple of the longitudinal grid size (5°). Preferably, the heating rate due to solar radiation absorption should be accumulated each time it is computed in the program. In Figure 13, the anomalously large short-wave heating rates

over Antarctica are due to the ice albedo error noted earlier (figs. 6, 7). On the global average, the 6-hr and $\frac{1}{2}$ -hr sampling gives nearly the same average heating rates due to short-wave absorption: 92.5 and 92.3 ly/day, respectively.

Of all the quantities examined, the latent heating, $C_1 + C_3$ in eq. (16), due to the parameterized convective condensation is the most sensitive to sampling frequency. Figures 15 and 16 show the average convective precipitation rate, P_c , as determined by both 6-hr and $\frac{1}{2}$ -hr

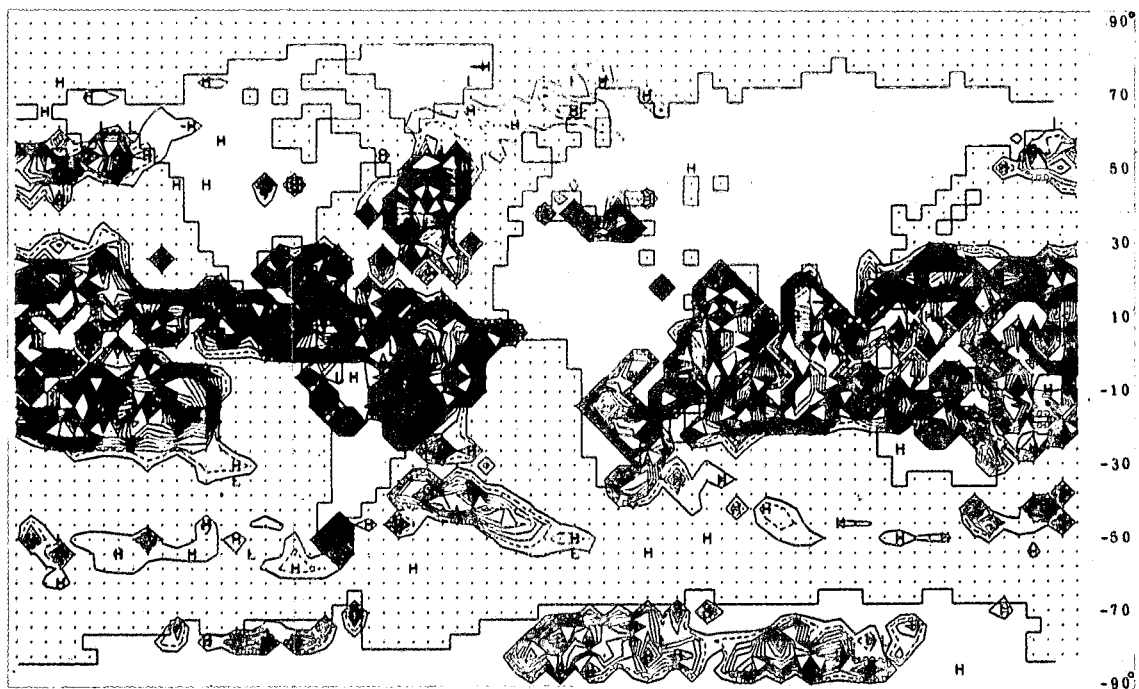


FIGURE 15.—The average rate of convective precipitation during 10 days of a January simulation, as given by sampling every 6 hr. The isolines are at intervals of 10 mm/day, with the 20-mm/day isoline dashed. The symbols H and L denote local relative maxima and minima.

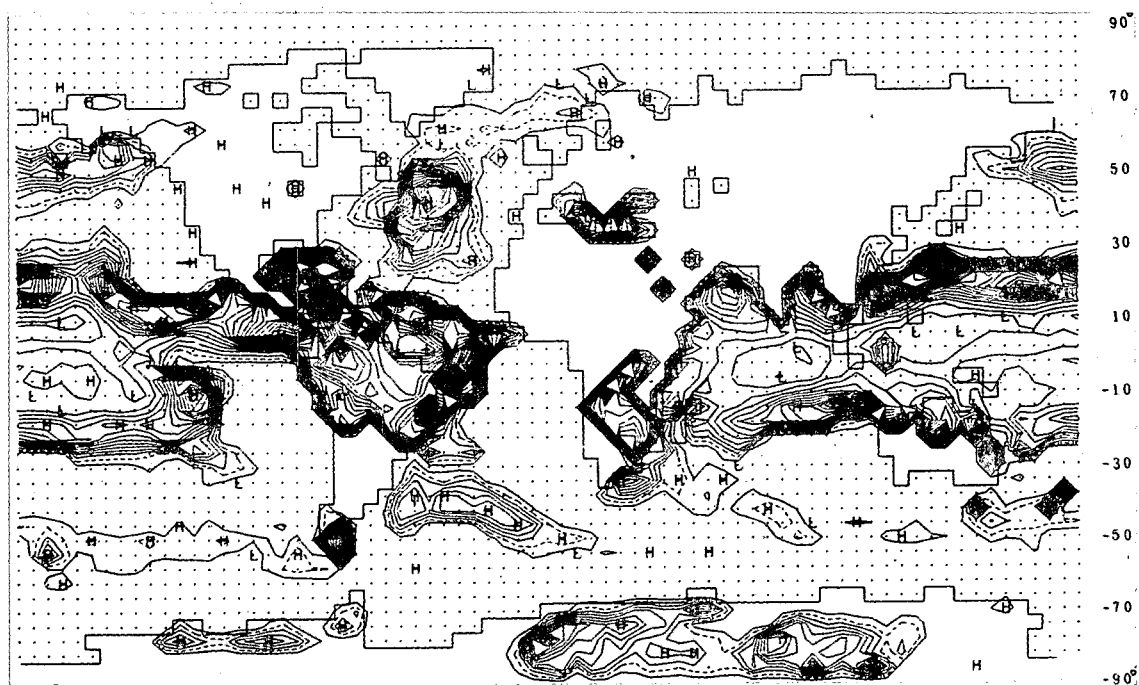


FIGURE 16.—Same as figure 15 for a sampling every 1/2 hr (the program's frequency of precipitation calculation).

sampling (over the selected 10-day period) to which the convective latent heating rate is proportional [eq (22)]. In the case of an accurate accumulation of all convective condensation ($\frac{1}{2}$ -hr sampling), there is a clear pattern to the average convective precipitation rate over the tropical oceans; maxima occur at approximately 20°N and 15°S , with secondary maxima over the midlatitude oceans. In the case of 6-hr sampling, the distribution over the tropi-

cal oceans becomes cellular and confused. This is due to the tendency of the simulated convective precipitation to occur at isolated points (or clusters of points) for short periods of time, usually much less than 6 hr. Such instantaneous condensation rates should not be applied to periods longer than those characteristic of the convection itself, which is here of the order of 1 hr. Sampling as infrequently as every 6 hr may also fail to adequately

portray the diurnal nature of convection over the continents during daytime.

This error is also noticeable in terms of the zonally averaged distribution shown in figure 17. In the lower latitudes, there is a sampling error of the order of 25 percent for the tropical convective rainfall, although, on the global average, the 6-hr and $\frac{1}{2}$ -hr sampling cases give nearly the same average convective precipitation rate (3.52 and 3.48 mm/day, respectively). Both sampling intervals show considerable convective precipitation over Antarctica (fig. 17); this is due to the model's inadvertent albedo

error for ice, as previously discussed in connection with figures 6 and 10.

Although it shows no appreciable sampling error as noted earlier, the distribution of the precipitation rate, $(PREC)L\pi/2g$, due to large-scale condensation is shown as determined from $\frac{1}{2}$ -hr accumulations (fig. 18). This precipitation is almost exclusively a middle- and high-latitude process, and shows maxima generally in the western portions of the midlatitude oceans. When added to the convective precipitation of figure 16 ($\frac{1}{2}$ -hr case), this distribution gives the total precipitation rate.

Due mainly to the sampling sensitivity of the simulated convection (and the associated latent heating and convective precipitation), both the total heating rate, \dot{H} , and the net rate of moisture addition, $E-P$, show a variation with sampling frequency. If these rates are constructed from data every 6 hr (instead of data from every $\frac{1}{2}$ hr, as in figs. 3 and 4), a distortion in low latitudes similar to that seen in figure 16 occurs. To obtain an accurate portrayal of the average total-heating and moisture-addition rates, one apparently must use the data from *each* step of the calculated convective process.

ACKNOWLEDGMENTS

Thanks are due Yale Mintz and Akio Arakawa of the Department of Meteorology, University of California at Los Angeles, for permission to use their two-level, general circulation model for the present simulation. I would also like to thank Yale Mintz for his constructive review of the present paper. Acknowledgment is due Robert Mobley and Al Nelson of Rand for their supervision of the computations and machine graphical output.

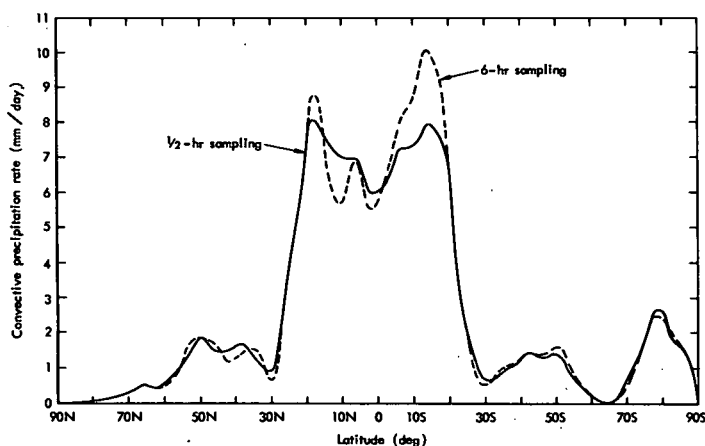


FIGURE 17.—The latitudinal distribution of the zonal average of the convective precipitation rate during 10 days of a January simulation. The solid curve is that given by $\frac{1}{2}$ -hr sampling, and the dashed curve that given by 6-hr sampling.

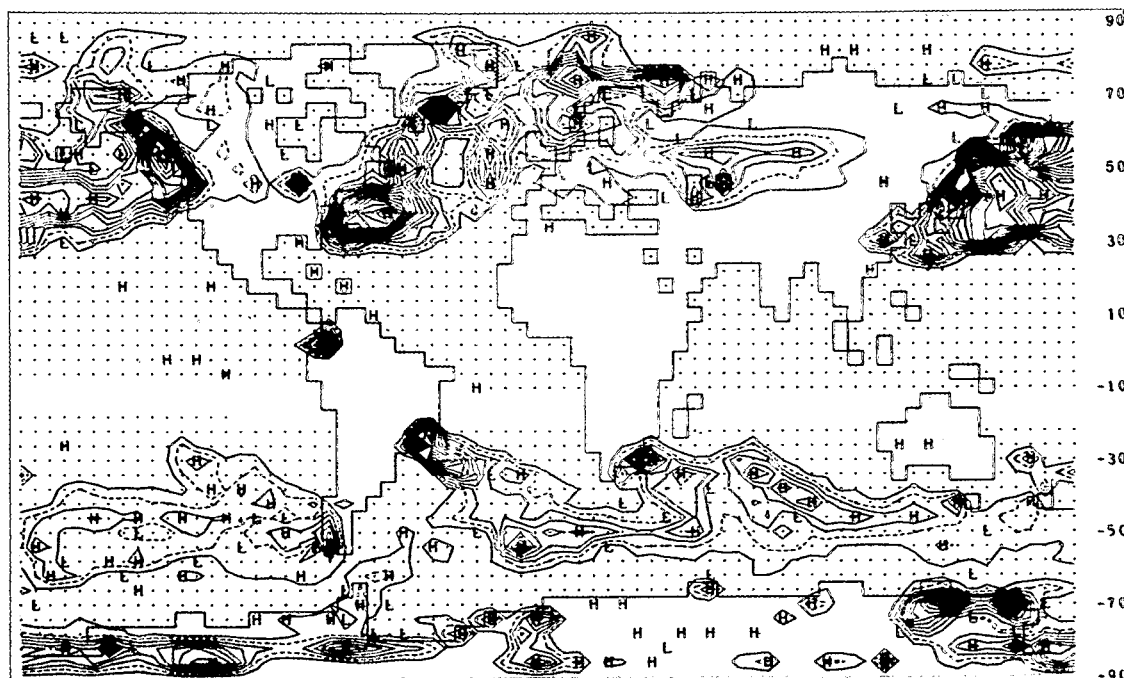


FIGURE 18.—Same as figure 16 for the average large-scale precipitation rate as given by $\frac{1}{2}$ -hr sampling. The isolines are at 5-mm/day intervals, with the 10-mm/day isoline dashed. Note that here the isoline interval is half that used in figures 15 and 16. The symbols H and L denote local relative maxima and minima.

REFERENCES

- Budyko, M. I. (Editor), *Atlas Liplovogo, Balansa Zemnogo Shara* (Guide to the Atlas of the Heat Balance of the Earth), Gidrometeoizdat, Moscow, U.S.S.R., 1963, 69 pp.
- Cressman, George P., "Improved Terrain Effects in Barotropic Forecasts," *Monthly Weather Review*, Vol. 88, Nos. 9-12, Sept.-Dec. 1960, pp. 327-342.
- Ellsaesser, H. W., "A Climatology of Epsilon (Atmospheric Dissipation)," *Monthly Weather Review*, Vol. 97, No. 6, June 1969, pp. 415-423.
- Gates, W. Lawrence, *The January Global Climate Simulated by the Two-Level Mintz-Arakawa Model: A Comparison with Observation*, R-1005-ARPA, The Rand Corporation, Santa Monica, Calif., Sept. 1972, 106 pp.
- Gates, W. Lawrence, Batten, E. S., Kahle, A. B., and Nelson, A. B., *A Documentation of the Mintz-Arakawa Two-Level Atmospheric General Circulation Model*, R-877-ARPA, The Rand Corporation, Santa Monica, Calif., Dec. 1971, 408 pp.
- Hellerman, S., "An Updated Estimate of the Wind Stress on the World Ocean," *Monthly Weather Review*, Vol. 95, No. 9, Sept. 1967, pp. 607-626.
- Jacobs, Woodrow, "The Energy Exchange Between Sea and Atmosphere and Some of Its Consequences," *Bulletin of the Scripps Institution of Oceanography*, University of California, La Jolla, Vol. 6, No. 2, 1951, 122 pp. (See pp. 27-122.)
- Kung, E. C., "Climatology of the Mechanical Energy Dissipation in the Lower Atmosphere over the Northern Hemisphere," Ph.D. Thesis, University of Wisconsin, Madison, 1963, 92 pp.
- London, Julius, "A Study of the Atmospheric Heat Balance," *Final Report*, Contract AF19(122)-165, Department of Meteorology and Oceanography, New York University, Bronx, N.Y., July 1957, 99 pp.
- Lvovitch, M. I., and Ovtchinnikov, S. P., *Fiziko-Geograficheskii Atlas Miro (Physical-Geographical Atlas of the World)*, Academy of Sciences, USSR, and Department of Geodesy and Cartography, State Geodetic Commission, Moscow, 1964, 298 pp.
- Möller, Fritz, "Vierteljahrskarten des Niederschlags für die Ganze Erde," *Petermann's Geographische Mitteilungen*, Vol. 95, No. 1, Justus Perthes, Gotha, East Germany, 1951, pp. 1-7.
- Newell, Reginald E., Vincent, Dayton G., Dopplick, T. G., Ferruzza, D., and Kidson, John W., "The Energy Balance of the Global Atmosphere," *Proceedings of the R.M.S./A.M.S. Joint Conference on the Global Circulation of the Atmosphere, August 25-29, 1969*, London, England, 1970, pp. 42-90.
- Sasamori, Takashi, London, Julius, and Hoyt, D. V., "Radiation Budget of the Southern Hemisphere," *NCAR Manuscript* 71-100, National Center for Atmospheric Research, Boulder, Colo., 1971, 49 pp.
- Schutz, C., and Gates, W. Lawrence, "Global Climatic Data for Surface, 800 mb, 400 mb: January," *Report R-915-ARPA*, The Rand Corporation, Santa Monica, Calif., Nov. 1971, 173 pp.

[Received July 17, 1972; revised December 18, 1972]